

## Self-Stabilization of Light Sails by Damped Internal Degrees of Freedom

M. Z. Rafat<sup>1,\*</sup>, Holger R. Dullin<sup>2</sup>, Boris T. Kuhlmeier<sup>1</sup>, Alessandro Tuniz<sup>1</sup>, Haoyuan Luo<sup>1</sup>, Dibyendu Roy<sup>1</sup>, Sean Skinner<sup>1</sup>, Tristram J. Alexander<sup>1</sup>, Michael S. Wheatland<sup>1</sup> and C. Martijn de Sterke<sup>1</sup>

<sup>1</sup>*School of Physics, University of Sydney, Sydney, NSW 2006, Australia*

<sup>2</sup>*School of Mathematics and Statistics, University of Sydney, Sydney, NSW 2006, Australia*

 (Received 21 June 2021; revised 5 November 2021; accepted 6 December 2021; published 7 February 2022)

We consider the motion of a light sail that is accelerated by a powerful laser beam. We derive the equations of motion for two proof-of-concept sail designs with damped internal degrees of freedom. Using linear stability analysis, we show that perturbations of the sail movement in all lateral degrees of freedom can be damped passively: the sail is asymptotically stable. This analysis also shows complicated behavior akin to that associated with exceptional points in PT-symmetric systems in optics and quantum mechanics. We show that the excess heat that is produced by the damping mechanism is likely to be substantially smaller than the expected heating due to the partial absorption of the incident laser beam by the sail.

DOI: [10.1103/PhysRevApplied.17.024016](https://doi.org/10.1103/PhysRevApplied.17.024016)

### I. INTRODUCTION

The task of sending spacecrafts to planets and other objects within our own solar system has become almost routine. The Breakthrough Starshot Initiative aims to expand our horizons beyond our own solar system to our closest neighbor, the Alpha Centauri system at a distance of 4.2 light years from Earth [1]. This enormous distance means that even the fastest man-made craft to date, the Parker Solar Probe (with a predicted top speed of 0.064% of the speed of light at its closest approach to the Sun [2]), would take about 6500 years to reach Alpha Centauri. A spacecraft accelerated by chemical fuel needs to carry a prohibitively large amount of fuel in order to reach speeds nearing any appreciable fraction of the speed of light. A natural candidate for an external source of energy is light, which was proposed decades ago [3,4]. This is the rationale for the approach taken by the Breakthrough Starshot Initiative. The aim is to send an ultralight sail craft with a payload to Alpha Centauri by accelerating it to about 20% of the speed of light using an Earth-based laser phased array [5]. This would allow the sail to reach Proxima Centauri and send signals back to Earth in about 26 years; all within a human lifetime. The sail is expected to have a mass of about one gram, with a payload that contains the detectors and electronics necessary to send a signal back to Earth having a similar mass [6]. There are numerous scientific and engineering challenges in every aspect of this grand vision, including laser array design [7], material choice [6,8], stability of the sail

under acceleration [9], heat management [6,10,11], and communication [12].

Diffraction of the accelerating beam and size limits on the laser array imply that a “reasonable” scheme to accelerate the sail to its final speed is as follows [5]. The total area of the sail is about  $10 \text{ m}^2$  and the net incoming laser intensity is approximately  $10 \text{ GW m}^{-2}$  from a laser array with aperture approximately 1 km. The sail is accelerated to approximately 20% of the speed of light over a distance of about 10 times the distance between Earth and the Moon in about 15 min. To increase momentum transfer, the sail material needs to have high refractive index, potentially in multiple layers [10,11], with low absorption in the laser wavelength range ( $1\text{--}1.5 \mu\text{m}$ ) and high absorption, and this high emissivity, at longer wavelengths (mid-infrared) to cool the sail through thermal radiation. The large surface area and low mass implies that the material must have low mass density [6]. A more modest setup may be used to accelerate probes to targets within our own solar system.

The severe limitation on the total mass of the craft precludes active stabilization and the enormous acceleration, about 66 000 times that due to Earth’s gravity, experienced by the sail implies short dynamical timescales that do not allow feedback loops for remote correction of the sail trajectory through adjustment of the laser beam profile. Instead, the craft needs to passively correct any perturbations that may cause it to exit the accelerating laser beam. A number of rigid body sail designs have been proposed that passively produce restoring forces on the sail toward the center of the beam [6,13–19]. These designs employ variations in geometry (e.g., flat, conical, parabolic, and

\*mohammad.rafat@sydney.edu.au

spherical), materials (various semiconducting materials), and surface structure (specular reflection, gratings, and metasurfaces) to manipulate the force (and torque) of the laser light on the sail. A salient feature in all of these designs is that the restoring forces lead to undamped oscillations of the orientation and displacement of the sail perpendicular to the laser beam. We refer to these collectively as *lateral oscillations* of the sail. These undamped lateral oscillations are problematic as they can potentially grow due to nonlinear coupling and/or if additional perturbations are imparted on the sail, for example due to inevitable deviations of the accelerating laser beam from its ideal beam shape and precise direction [7]. To overcome this problem, a damping term was added by Srivastava *et al.* [13] to the equations of motion, whereas Salary and Mosallaei [14] discussed potential damping of lateral motion of the sail through Doppler damping. However, Srivastava *et al.* do not discuss a physical implementation, and the mechanism and effectiveness of Doppler damping require further study.

We propose and investigate an alternative approach that consists of incorporating damped internal degrees of freedom in the sail. The aim is to couple the lateral oscillations of the sail to the damped internal degrees of freedom, causing the lateral oscillations to decay. This principal has been used extensively in many areas of engineering, including damping of oscillations of high rise buildings caused by earthquakes and high winds [20,21], vibration of racing cars (Renault R26) and spacecrafts (NASA's Ares solid fuel booster). In a light sail, incorporating a damped internal degree of freedom could be challenging, and the implementation would depend on the exact sail geometry, which is still being debated. In a geometry such as IKAROS [22], which has several sails connected by a frame, one could have damped hinges on the frame [Fig. 1(a)]. For the Starshot project, most light sails proposed have been modeled as flat rigid sheets with a central

payload chip or a distributed payload. A central payload could be attached to the chip through an elastic and damped connection [Fig. 1(b)] with the relative motion between sail and payload being the damped internal degree(s) of freedom. For distributed payloads, the elasticity of the sail itself could be used as damped internal degrees of freedom [Fig. 1(c)] with damping coming for example from passive magnetic induction or phonon scattering. One could even imagine multiple sheets connected by elastoviscous media with higher damping [Fig. 1(d)] or distributed damped cantilevers [Fig. 1(e)].

Here we consider two sails with different internal degrees of freedom that have been incorporated in a rigid two-dimensional (2D) geometry [Fig. 2(a)]. We refer to these two proof-of-concept designs as the moveable mass (MM) sail [Fig. 2(b)] and moving arms (MA) sail [Fig. 2(c)]. For both of these sail designs, the nonrelativistic equations of motion can be derived in closed form. We find that the MM sail design is effective in damping lateral oscillations, whereas the MA sail design is not. This shows that the internal degrees of freedom need to be chosen with care. The dissipated energy adds to the energy that is inevitably absorbed by the sail from the laser beam, and which needs to be lost as thermal radiation. We show that the heat generated through damping of lateral oscillations of the sail is likely to be smaller than the absorbed laser power. We therefore conclude that the damping of undesired sail motion by dissipative internal degrees of freedom is realistic and deserves further investigation.

The outline of this paper is as follows. In Sec. II we introduce the rigid sail, as well as the MM and MA sails. The equations of motion for the MM sail are obtained in Sec. III and its linear stability is analyzed in Sec. IV. Our numerical results are presented in Sec. V and we discuss and summarize our results in Sec. VI. The stability of the MA sail and various other supporting information are presented in the appendices.

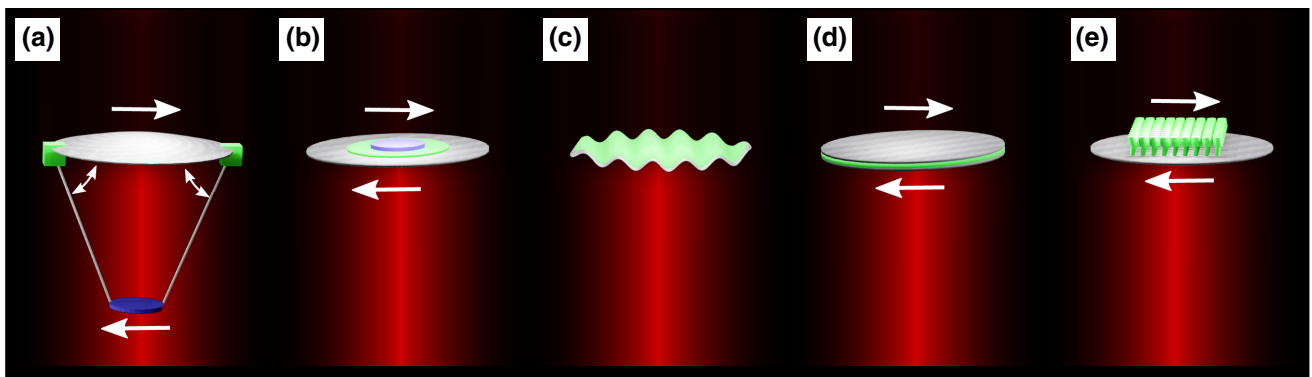


FIG. 1. Examples of implementations of damped internal degrees of freedom for light sails. Green represents the elastic damped medium; blue represents the payload (when not distributed on the sail); red represents the laser beam. (a) Damped hinges; (b) central payload attached by viscoelastic medium; (c) damped modes of vibration; (d) dual layers separated by viscoelastic medium; (e) distributed damped cantilever. Arrows represent the examples of damped transverse motion. Features are not to scale.

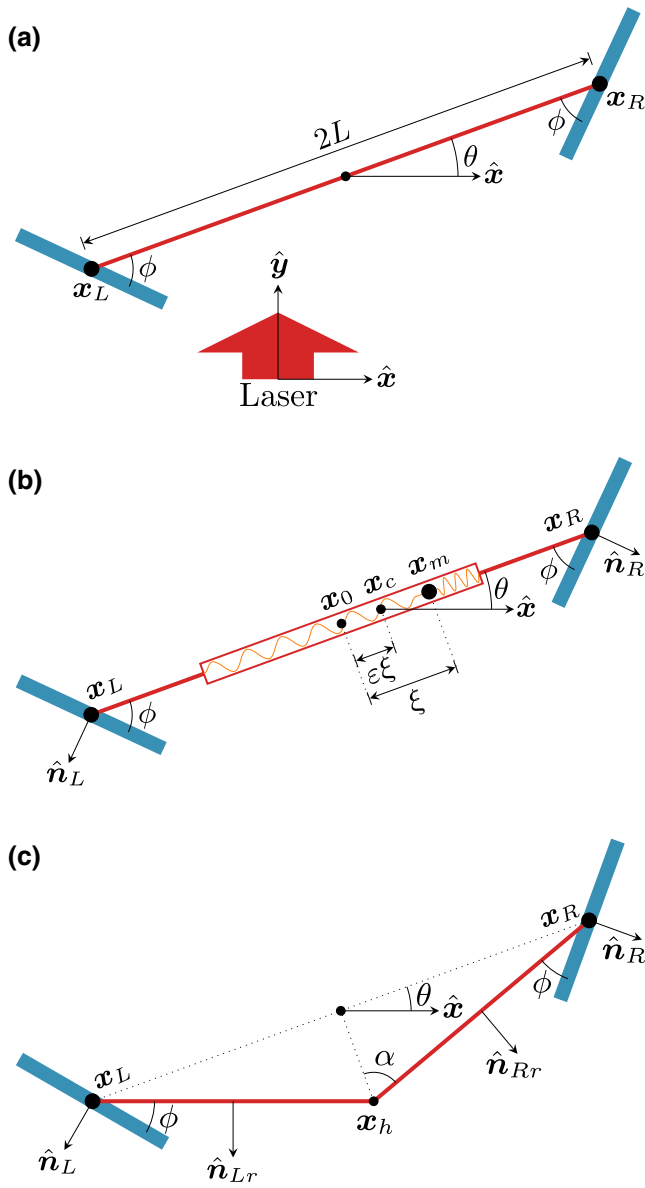


FIG. 2. Sail schematics. (a) Simple, rigid 2D sail consisting of two mirrors at positions  $\mathbf{x}_{L,R}$  connected by a massless rod of length  $2L$ ; the mirrors make an angle  $\phi$  with the rod. Angle  $\theta$  gives the orientation of the sail with respect to the incoming laser beam (red arrow). (b) Moveable mass sail with a moveable point mass that is connected to the rest of the sail by damped springs. The moveable mass is at  $\mathbf{x}_m$  at a distance  $\xi$  from the center of the sail at  $\mathbf{x}_0$ ; the center of mass is displaced from  $\mathbf{x}_0$  by  $\epsilon\xi$  to  $\mathbf{x}_c$ ; and  $\hat{\mathbf{n}}_{L,R}$  are the normals to the mirrors. (c) Moving arms sail in which the connecting rod has a damped hinge at the center at  $\mathbf{x}_h$ ,  $\alpha$  is the half-angle between the rods, with normals  $\hat{\mathbf{n}}_{Lr}$  and  $\hat{\mathbf{n}}_{Rr}$ .

## II. SAIL DESIGNS

To analyze the possibility of damping through internal degrees of freedom, we start from arguably the simplest sail design exhibiting restoring forces toward the center of the laser beam. Our emphasis here is to show that a

damped internal degree of freedom can damp any lateral perturbations and return the sail to its equilibrium point instead of focusing on practically viable mechanisms for producing restoring forces. A spherical sail in a doughnut beam has been shown to be marginally stable within the beam [15]. Marginal stability refers to the situation where the system is neither unstable nor asymptotically stable: small perturbations from its equilibrium neither grow nor decay over time. Considering finite two-dimensional sections of such a sphere provides a simpler geometry, still exhibiting marginal stability, shown in Fig. 2(a): two mirrors, each with mass  $m_1$  located at  $\mathbf{x}_L$  (left mirror) and  $\mathbf{x}_R$  (right mirror) are connected by a massless rigid rod of length  $2L$ . The mirrors are at angle  $\phi$  with the connecting rod, which in turn has an angle  $\theta$  (orientation angle of the sail) with the  $x$  axis of the coordinate frame in which the laser is at rest—the *laser frame*. Our equations are written in this frame. We consider perfect specular reflection by the mirrors subject to a laser beam profile, pointing along the positive  $y$  axis, given by

$$I(\mathbf{x}) = I_0[\delta_0 + (\mathbf{x} \cdot \hat{\mathbf{x}}/L)^2], \quad (1)$$

where  $\delta_0 \geq 0$  is a dimensionless constant,  $\mathbf{x}$  is the position vector, and  $\hat{\mathbf{x}}$  is the unit vector along the  $x$  axis of the laser frame. This beam profile may be viewed as the lowest-order approximation (valid for small displacements of the sail from the center of the beam) to an annular beam [23] or to a Laguerre-Gaussian mode laser beam with a nonzero orbital angular momentum number when  $\delta_0 = 0$  [24].

We assume that the laser is always focused on the sail (so that the beam profile does not depend on the distance along the  $y$  axis from the laser) and ignore relativistic effects, in particular the Doppler shift of the laser light [25–29] so that the momentum transfer for each photon is independent of the speed of the sail. We assume point mirrors in the sense that the intensity of the laser is approximated to be uniform across the projected area of each mirror. The model can easily be made more realistic by replacing the point mirrors with spatially extended gratings [9,13], but our focus here is the dissipation mechanism of the lateral motions of the sail.

The stability of this simple sail can be understood as follows. If the sail shifts to the right compared to the center of the beam, the intensity at the right mirror increases, while that at the left mirror decreases, creating a net restoring force. Similarly, if  $\theta$  is positive, the cross section of the left mirror intercepting the beam is larger than that of the right mirror, leading to a net restoring torque. A more complete linear stability analysis (see Appendix B) shows that this geometry is indeed stable, but not damped, i.e., it is marginally stable, similar to the more complicated designs considered in the literature, e.g., by Ilic and Atwater [9].

### A. Moveable mass sail

Figure 2(b) shows the first modification of the sail shown in Fig. 2(a) in which we introduce a damped internal degree of freedom by incorporating a moveable mass. The connecting rod now includes a housing that is located symmetrically about the center of the sail at  $\mathbf{x}_0$  between the mirrors. The housing contains a moveable point mass  $m_2$  located at  $\mathbf{x}_m$  with its movement constrained along a straight line between the mirrors at  $\mathbf{x}_L$  and  $\mathbf{x}_R$ . The mass is connected to the two ends of the housing by damped massless springs. The extension and compression of each spring is denoted by  $\xi$  and is measured from its equilibrium at  $\mathbf{x}_0$ . The center of mass of the sail is at  $\mathbf{x}_c$  at a distance  $\varepsilon\xi$  from  $\mathbf{x}_0$ , where  $\varepsilon = m_2/M$  with  $M = 2m_1 + m_2$ .

The springs provide a restoring force on the moveable mass at  $\mathbf{x}_m$  toward its equilibrium position at  $\mathbf{x}_0$ . In the frame in which the mirrors are at rest, when the mass is perturbed, it oscillates about  $\mathbf{x}_0$  along the length of the connecting rod. In the laser frame the mirrors and the mass counter oscillate about  $\mathbf{x}_c$  such that the center of mass does not accelerate in the absence of a net nonzero external force.

As shown in Fig. 1, the restoring force and the damping could be provided by a number of different physical mechanisms. However, our analysis is agnostic to these, as long as the nature of the restoring and damping forces are not drastically different. For convenience, we refer to the restoring and damping forces as provided by springs in both MM and MA sails.

### B. Moving arms sail

Figure 2(c) shows the second sail design that we consider. In this MA sail design, the rigid rod has a hinge halfway between the mirrors at  $\mathbf{x}_h$  with opening half angle  $\alpha$ . The total mass for this sail is  $M = 2m_1$ . A massless damped torsion spring at the hinge provides a torque on the arms with equilibrium at  $\alpha = \alpha_0$ . When the MA sail is perturbed, the arms oscillate about the equilibrium opening half angle  $\alpha_0$  and cause the center of mass of the sail to oscillate along the line joining  $\mathbf{x}_c$  and  $\mathbf{x}_h$  in the laser frame.

## III. EQUATIONS OF MOTION

We now derive and discuss the equations of motion of the MM sail, whereas the equations of motion for the MA sail are discussed in Appendix C.

### A. Forces

We denote the coordinates of the center of mass of the sail as  $\mathbf{x}_c = [x, y]$ , so that

$$\mathbf{x}_{L,R} = \mathbf{x}_c \mp (L \pm \varepsilon\xi)\hat{\mathbf{r}}, \quad \mathbf{x}_m = \mathbf{x}_c + (1 - \varepsilon)\xi\hat{\mathbf{r}}, \quad (2)$$

where  $\hat{\mathbf{r}} = [\cos\theta, \sin\theta]$  is a unit vector and  $\mathbf{x}_{L,R}$  and  $\mathbf{x}_m$  are as discussed in Sec. II. The force exerted by the laser on the sail is then given by

$$\mathbf{F}_{\text{laser}} = -\frac{2A}{c} \sum_{i=L,R} I(\mathbf{x}_i) (\hat{\mathbf{n}}_i \cdot \hat{\mathbf{y}})^2 \hat{\mathbf{n}}_i, \quad (3)$$

where  $A$  is the area of the point mirrors,  $c$  is the speed of light in vacuum,  $I(\mathbf{x})$  is the laser intensity, as given by Eq. (1), and  $\hat{\mathbf{n}}_{L,R} = [\sin(\theta \mp \phi), -\cos(\theta \mp \phi)]$  are the unit normals to each mirror, as shown in Fig. 2(b). In Eq. (3) one power of  $(\hat{\mathbf{n}}_i \cdot \hat{\mathbf{y}})$  arises from the projection of the area of the mirrors and the other from transfer of the momentum of photons to the mirrors. The choice of unit normals to the mirrors require that  $\phi$  and  $\theta$  must satisfy  $0 < \phi \pm \theta < \pi/2$ , so that the laser is incident on the reflecting surface of the mirrors and the force generated is pointing toward the center of the beam—a restoring force.

The forces provided by the springs (including the damping force) on the mirrors and the moveable mass are

$$\mathbf{F}_{sL,R} = (k\xi + \Gamma\dot{\xi})\hat{\mathbf{r}}, \quad \mathbf{F}_{sm} = -2(k\xi + \Gamma\dot{\xi})\hat{\mathbf{r}}, \quad (4)$$

where  $k$  is the spring constant of each of the springs,  $\Gamma$  is the damping coefficient, and time derivatives are denoted by a dot. Note that the internal forces add to zero in the inertial laser frame.

## B. Equations of motion

The equations of motion of the sails may be obtained using the Newton-Euler approach or using D'Alembert's principle (see Appendix A 1) as

$$\ddot{x} = -\bar{I}(\mathbf{x}_L) \cos^2(\theta - \phi) \sin(\theta - \phi) - \bar{I}(\mathbf{x}_R) \cos^2(\theta + \phi) \sin(\theta + \phi), \quad (5a)$$

$$\ddot{y} = \bar{I}(\mathbf{x}_L) \cos^3(\theta - \phi) + \bar{I}(\mathbf{x}_R) \cos^3(\theta + \phi), \quad (5b)$$

$$\ddot{\theta} = -\frac{2\varepsilon\bar{\xi}\dot{\xi}\dot{\theta}}{1 + \varepsilon\bar{\xi}^2} - \frac{\cos\phi[(1 + \varepsilon\bar{\xi})\bar{I}(\mathbf{x}_L) \cos^2(\theta - \phi) - (1 - \varepsilon\bar{\xi})\bar{I}(\mathbf{x}_R) \cos^2(\theta + \phi)]}{(1 - \varepsilon)(1 + \varepsilon\bar{\xi}^2)}, \quad (5c)$$

$$\ddot{\xi} = \bar{\xi} \dot{\theta}^2 - \frac{2\bar{k}\bar{\xi} + 2\bar{\Gamma}\dot{\bar{\xi}}}{\varepsilon(1-\varepsilon)} - \frac{\sin\phi[\bar{I}(\mathbf{x}_L)\cos^2(\theta-\phi) - \bar{I}(\mathbf{x}_R)\cos^2(\theta+\phi)]}{1-\varepsilon}, \quad (5d)$$

where  $I(\mathbf{x}_i) = I_0\bar{I}(\mathbf{x}_i)$  and a bar denotes a nondimensionalized quantity. We nondimensionalize using mass, length, and time scaling factors  $m_s = M$ ,  $x_s = L$ , and  $t_s = \sqrt{MLc/2I_0A}$ , respectively. The scaling factors of the spring constant and damping coefficient of the MM sail are respectively  $k_s = m_s/t_s^2$  and  $\Gamma_s = m_s/t_s$ . Our results are independent of the specific values of the parameters that appear in the scaling factors; however, we provide nominal values in Appendix A 3 that we use to obtain our dimensional results.

Equation (5) shows that the  $x$ ,  $y$ , and  $\theta$  coordinates of the MM sail do not depend directly on the restoring and damping forces provided by the springs. The damping is indirect through  $\xi$  and/or its time derivative. All terms multiplying  $\bar{I}(\mathbf{x}_{L,R})$  result from the force exerted by the laser beam on the mirrors. The first term in Eq. (5c) can be interpreted as the Coriolis effect and arises due to time dependence of the moment of inertia of the sail, whereas the first term in Eq. (5d) can be interpreted as the centrifugal effect. In the Lagrangian framework such effects result from the time dependence of the nondiagonal mass matrix in the expression of the kinetic energy of the sail. Both Coriolis and centrifugal terms arise as we are no longer dealing with a rigid body system. The equations of motion of the MM sail are singular when  $\varepsilon = 0$  (for  $m_2/m_1 \rightarrow 0$ ) and  $\varepsilon = 1$  (for  $m_2/m_1 \rightarrow \infty$ ), but these limits are not of interest. We show in Sec. IV that, for the sail to be stable, we require  $\phi$  to be larger than some minimum value. For  $\theta \mp \phi = \pi/2$ , the projected area of the left or right mirror goes to zero, leading to zero force due to the laser on the mirror. We note that the equations of motion of the simple sail, shown in Fig. 2(a), may be obtained from those of the MM sail by ignoring Eq. (5d) and taking the limit  $\varepsilon \rightarrow 0$  in Eqs. (5a)–(5c).

Henceforth, except where explicitly stated, we work with nondimensionalized quantities and drop the bar for simplicity of notation.

#### IV. STABILITY ANALYSIS

We analyze the stability of the MM sail by linearizing Eq. (5) by expanding about the equilibrium point  $(x, \theta, \xi, \dot{x}, \dot{\theta}, \dot{\xi}) = \mathbf{0}$ . For the sail to be asymptotically stable with damped lateral motion, we require that the eigenvalues of the coefficient matrix have negative real parts so that the general solution

$$\mathbf{v} = \sum_s c_s e^{\Re\lambda_s t} e^{i\Im\lambda_s t} \mathbf{v}_s$$

decays with time. Here coefficients  $c_s$  are determined by the initial conditions,  $\mathbf{v}_s$  are eigenvectors corresponding to eigenvalues  $\lambda_s$ , and  $s$  runs over all nontrivial eigenmodes. Marginal stability corresponds to the case where  $\Re\lambda_s = 0$ .

Linearizing the equations of motion of the MM sail results in a characteristic polynomial of degree eight (see Appendix D) with six nontrivial eigenvalues. The two trivial eigenvalues result because the equations of motion do not depend on coordinate  $y$  and its time derivative. This is a consequence of our assumption that the laser beam profile has no dependence on  $y$  and our neglect of the Doppler shift of the laser wavelength (so that there is no dependence on  $\dot{y}$ ). The characteristic polynomial of the MM sail cannot be solved analytically. We employ the Routh-Hurwitz criterion [30] to obtain a set of necessary and sufficient conditions for all nontrivial solutions of the characteristic polynomial to have nonzero negative real parts. These conditions are found to be

$$\begin{aligned} \delta_0 \geq 0, \quad 0 < \varepsilon < 1, \quad \Gamma > 0, \quad k > k_{\min}, \quad \text{and} \\ \phi_{\min} < \phi < \pi/2, \end{aligned} \quad (6)$$

where

$$\begin{aligned} k_{\min} &= (1 + \delta_0)\varepsilon^2 \cos^2 \phi \sin \phi \quad \text{and} \\ \phi_{\min} &= \cos^{-1} \left[ 1 - \frac{9 + 6\delta_0 + \delta_0^2}{19 - 4\varepsilon + 14\delta_0 + 3\delta_0^2} \right]^{1/2}. \end{aligned} \quad (7)$$

We observe, as expected, that a nonzero damping coefficient  $\Gamma$  is necessary for the sail to be stable (and damped). The minimum value of  $\phi$  increases with increasing  $\varepsilon$  and decreases with increasing  $\delta_0$ . This respectively results in increasing and decreasing the restoring component ( $x$  component) of the laser force, while doing the opposite for the net force. The minimum spring constant  $k$  increases with minimum laser intensity  $\delta_0$  and mass ratio  $\varepsilon$  and decreases with increasing  $\phi$  (increasing laser restoring force and decreasing total laser force). The conditions for minimum  $k$  and  $\phi$  ensure that a sufficient restoring force is provided on the moveable mass and on the sail, respectively.

Equation (6) gives a wide range of parameters over which all eigenmodes are damped. That is, for which any lateral displacement of the sail (including rotations) are damped provided the perturbations from equilibrium are sufficiently small for nonlinear effects to be insignificant. The MM sail is therefore asymptotically stable in contrast to the marginally stable sails in the existing literature [6,13,15–19].

Figure 3 shows the real (top row) and imaginary (bottom row) parts of the nontrivial eigenvalues as a function of damping coefficient  $\Gamma$  for parameter values given in the figure caption. All eigenvalues have negative real parts and are purely real or occur in complex conjugate pairs, as expected. As  $k/k_{\min}$  is increased, the imaginary parts of  $\lambda_{1-4}$  are relatively unaffected, with  $0.5 \lesssim |\Im\lambda_{1,2}| \lesssim 0.52$  and  $1.6 \lesssim |\Im\lambda_{3,4}| \lesssim 1.7$ , while  $|\Im\lambda_{5,6}|$  increase from zero at  $k/k_{\min} = 1$ . However,  $\Im\lambda_{5,6}$  is nonzero only for small  $\Gamma$  up to the bifurcation point (indicated by green circles) of  $\lambda_{5,6}$  where  $\lambda_{5,6}$  becomes purely real. Past the bifurcation point, the magnitude of  $\Im\lambda_5$  decreases toward zero while that of  $\Im\lambda_6$  continues to increase with  $\Gamma$ . The real parts of  $\lambda_{1,2}$  and  $\lambda_{3,4}$  remain relatively unaffected as  $k/k_{\min}$  is increased except near values where these eigenvalues coalesce (indicated by magenta circles) in the complex plane with  $\lambda_{5,6}$  when  $k/k_{\min} \approx 4.69$  and  $\approx 33.7$ , respectively, as seen in columns (b) and (c) of Fig. 3, and the absolute value of their real parts are maximized.

The modes corresponding to  $\lambda_{5,6}$  become purely decaying modes past the bifurcation point for larger  $\Gamma$ , while the other modes remain oscillatory and decaying. This may be viewed as modes corresponding to  $\lambda_{5,6}$  becoming overdamped for sufficiently large  $\Gamma$  while the other modes remain underdamped. The eigenvectors associated with  $\lambda_{5,6}$  are dominated by the mass-spring system, while the mass-spring system is weakly coupled to the other modes. The coalescence points then may be viewed as locations where the mass-spring system is strongly coupled to the other modes of the system, leading to increased dissipation rates in the corresponding modes.

The magnitude of the troughs of the real parts of the relevant eigenvalues increase to a maximum at coalescence points and then decrease and move to larger  $\Gamma$  with increasing  $k/k_{\min}$ . These coalescence points indicate resonance points between these eigenmodes where they share a common dissipation rate and oscillation frequency. This implies that, for damping lateral motions of the sail, the

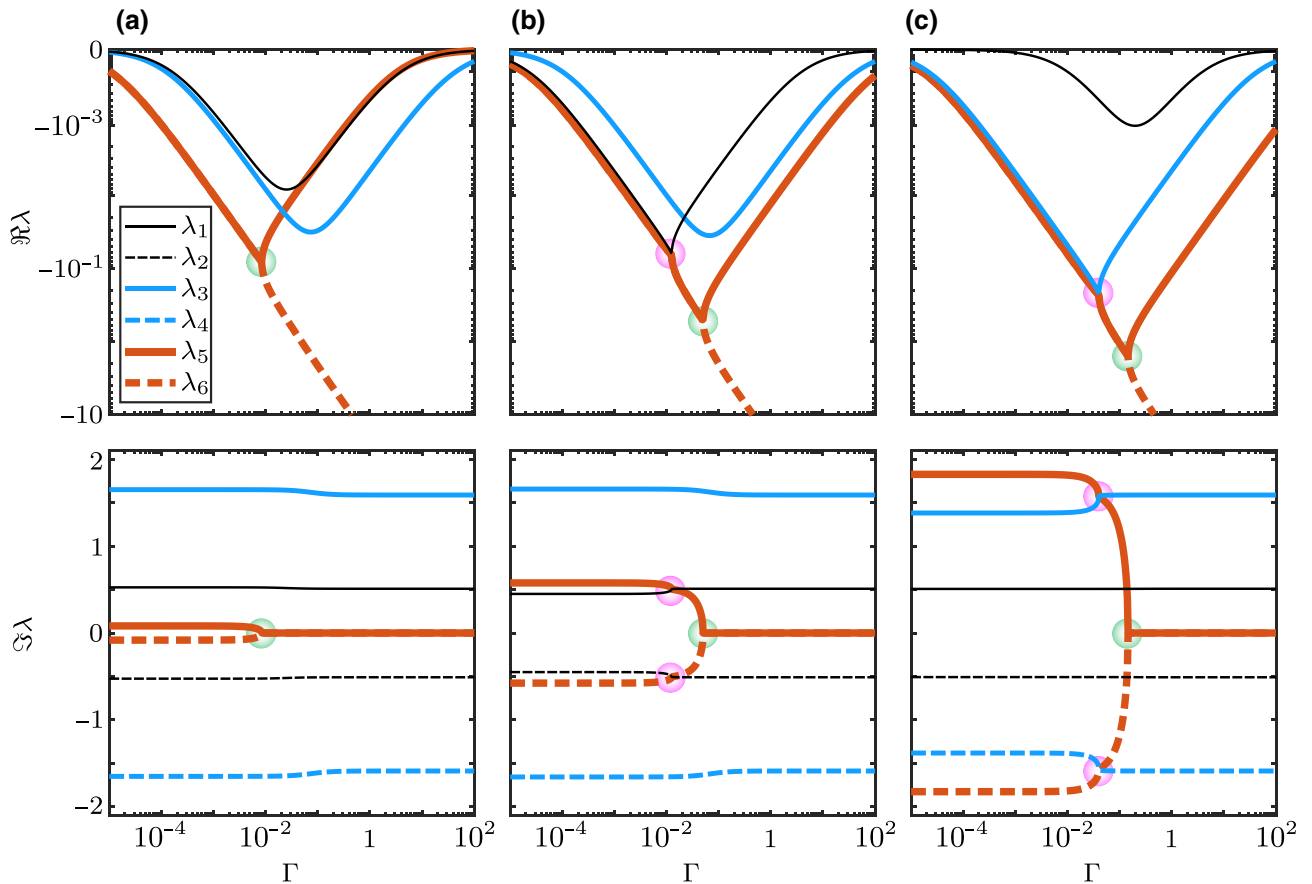


FIG. 3. Stability analysis: eigenvalues of the MM sail. Real (top row) and imaginary (bottom row) parts versus  $\Gamma$  for  $\delta_0 = 0.1$ ,  $\varepsilon = 0.1$ ,  $\phi/\phi_{\min} = 1.15$ , and  $k/k_{\min} = 1.1$  [column (a)], 4.6869 [column (b)], and 33.717 [column (c)]. Different eigenvalue pairs are shown using different colors, line thicknesses, and styles (see the legend). The vertical axis of the top row uses a bisymmetric logarithmic scaling with range  $|\Re\lambda| \leq 1$  represented over ten decades. The green and magenta circles indicate the bifurcation and coalescence points, respectively.

optimal values of  $k/k_{\min}$  and  $\Gamma$  are possibly those that correspond to the intersections of  $\lambda_{1,2}$  and  $\lambda_{5,6}$  as eigenmodes corresponding to  $\lambda_{1,2}$  have the slowest decay rates. This choice also avoids (potential) high-frequency oscillations of the sail corresponding to nonzero  $\Im\lambda_{5,6}$  when  $k/k_{\min}$  is large, specially when past the intersections of  $\lambda_{3,4}$  and  $\lambda_{5,6}$ . However, the precise choice of optimal values of the parameters leading to the fastest decay rate is a nontrivial exercise as the coordinates of coalescence points in the  $(k, \Gamma)$  plane also depend on  $\delta_0$ ,  $\varepsilon$ , and  $\phi$ . In general, the coalescence points move to lower  $k$  and higher  $\Gamma$  coordinates with increasing  $\delta_0$  and  $\phi$  and to lower  $k$  and higher  $\Gamma$  with  $\varepsilon$ . For  $k/k_{\min} \gtrsim 4.7$ , the bifurcation of  $\Im\lambda_{5,6}$  occurs at  $\Gamma \approx \sqrt{k/k_{\min}}/40$  for the parameters used in the figure; the scaling  $\propto \sqrt{k/k_{\min}}$  is maintained when  $\delta_0$ ,  $\varepsilon$ , and  $\phi$  are varied.

The bifurcation of  $\lambda_{5,6}$  as a function of  $k$  and  $\Gamma$  are similar to the appearance of exceptional points in PT-symmetric systems in quantum mechanics and optics [31–33], for example that of a passive, lossy plasmonic-dielectric waveguide model [34]. The spring constant  $k$  plays the role of the coupling constant, with  $k_{\min}$  being its critical value, while  $\Gamma$  corresponds to the loss in the supporting waveguide. Previous reports in passive optical two-mode systems [34] showed that the exceptional point is associated with the largest overall dissipation. In this mechanical six-mode system, the topology of the eigenspace is significantly more complicated and the choice of optimal parameters is not obvious. In the neighborhood of the exceptional and coalescence points, PT-symmetric systems may exhibit rich physics [35] (including exchange of energy between eigenmodes) and possible chiral behavior [36]. These are determined from a detailed analysis of the topology of the Riemann surfaces [37–39], which is beyond the scope of the current paper.

When the conditions given in Eq. (6) are satisfied, we are guaranteed to have an asymptotically stable equilibrium. However, the neighborhood of the equilibrium where linear stability is applicable could be very small as (typically small factors)  $k$  and  $\Gamma$  multiply linear terms in Eq. (5), i.e., there is the potential danger of entering the nonlinear regime for seemingly small perturbations about the equilibrium. We must choose  $\delta_0$ ,  $\varepsilon$ ,  $\phi$ ,  $k$ , and  $\Gamma$  judiciously if a specific damping rate of the lateral oscillations of the sail is desired and/or if lateral perturbations in a specific neighborhood of the equilibrium are to be damped; the latter is not always guaranteed.

Figure 4 shows plots of  $x$ ,  $y$ ,  $\theta$ ,  $\xi$ , and their derivatives versus time  $t$  for the same parameter values used in column (a) of Fig. 3 with  $\Gamma = 0.04$  and initial conditions  $(x_0, \theta_0, \dot{x}_0, \dot{\theta}_0) = (0.5, 0.35, 0.15, 0.15)$ , calculated by integrating the full nonlinear equations of motion, Eq. (5) (see Appendix A 2). The vertical and horizontal axes have been scaled for convenience as shown. The choice of

$(x_0, \theta_0) = (0.5, 0.35)$  is somewhat arbitrary and the additional perturbations in  $\dot{x}_0$  and  $\dot{\theta}_0$  increase  $x$  and  $\theta$  in the absence of damping. For comparison, Ilic and Atwater [9] used  $(x_0, \theta_0, \dot{x}_0, \dot{\theta}_0) = (0.5, 0.1, 0, 0)$  to demonstrate the marginal stability of the sail they considered. It is evident that all lateral motions of the MM sail are damped over time. The motion along the  $y$  axis has (almost) constant acceleration and is decoupled in this (mostly) linear regime with  $y(t) \approx [(1 + \delta_0) \cos^3 \phi] t^2$ . This decoupling implies that the damping mechanism significantly affects only the lateral components of the sail motion, as desired.

The lateral oscillations of the sail are irregular in the initial phase of the motion and become more regular with increasing time as the fastest decaying modes damp out. The quantities  $x$ ,  $\theta$ ,  $\dot{x}$ , and  $\dot{\theta}$  reach their maximum (absolute) values at times  $t \approx 6.1, 3.2, 21$ , and  $11$ , respectively, and reduce to  $1/e$  of their maximum values after the *damping time*  $\Delta t_{1/e} \approx 58, 98, 91$ , and  $74$ . For the nominal parameter values (see Appendix A 3), these correspond to dimensional damping times  $\Delta t_{1/e} \approx 0.17, 0.29, 0.27$ , and  $0.22$  s, respectively. The decay time for the lateral perturbations of the sail is thus quite short compared to the nominal acceleration time of approximately 900 s. The longest surviving oscillations have (nondimensional) angular frequency  $\omega \approx 0.52$  corresponding to  $\Im\lambda_{1,2}$  in column (a) of Fig. 3. This corresponds to a dimensional angular frequency of approximately  $68 \text{ rad s}^{-1}$ . The other four eigenmodes have dimensional oscillation frequencies of  $\omega_{3,4} \approx 560 \text{ rad s}^{-1}$  and  $\omega_{5,6} \approx 28 \text{ rad s}^{-1}$ . The oscillations of the sail due to  $\omega_{5,6}$  may be avoided through an appropriate choice of parameters, as discussed above, and  $\omega_{3,4}$  may be tuned by changing the sail parameters that affect scaling factor of time,  $t_s$ .

The stability analysis of the MA sail (see Appendix C) shows that, unlike the MM sail, at best it can have two damped eigenmodes and four undamped ones. The undamped modes of the MA sail do not dissipate when excited and hence the MA sail is not asymptotically stable. Furthermore, any deviations from a narrow range of parameter values lead to the emergence of growing modes and instability.

## V. NUMERICAL RESULTS

The results presented in the previous section are for a single set of values of sail and laser parameters  $\delta_0$ ,  $\varepsilon$ ,  $\phi$ ,  $k$ , and  $\Gamma$  and for a single set of initial conditions  $(x_0, \theta_0, \dot{x}_0, \dot{\theta}_0)$ . Here we demonstrate the asymptotic stability of the MM sail by calculating the damping time of the perturbations for an ensemble of initial conditions and parameter values. We choose a default set of parameters  $\delta_0 = 0$ ,  $\varepsilon = 0.1$ ,  $\phi/\phi_{\min} = 1.05$ ,  $k/k_{\min} = 1.1$ , and  $\Gamma = 10^{-2}$  with, using Eq. (7),  $\phi_{\min} \approx 0.769$  and  $k_{\min} \approx 3.45 \times 10^{-3}$  for the chosen values of  $\delta_0$  and  $\varepsilon$ , and vary

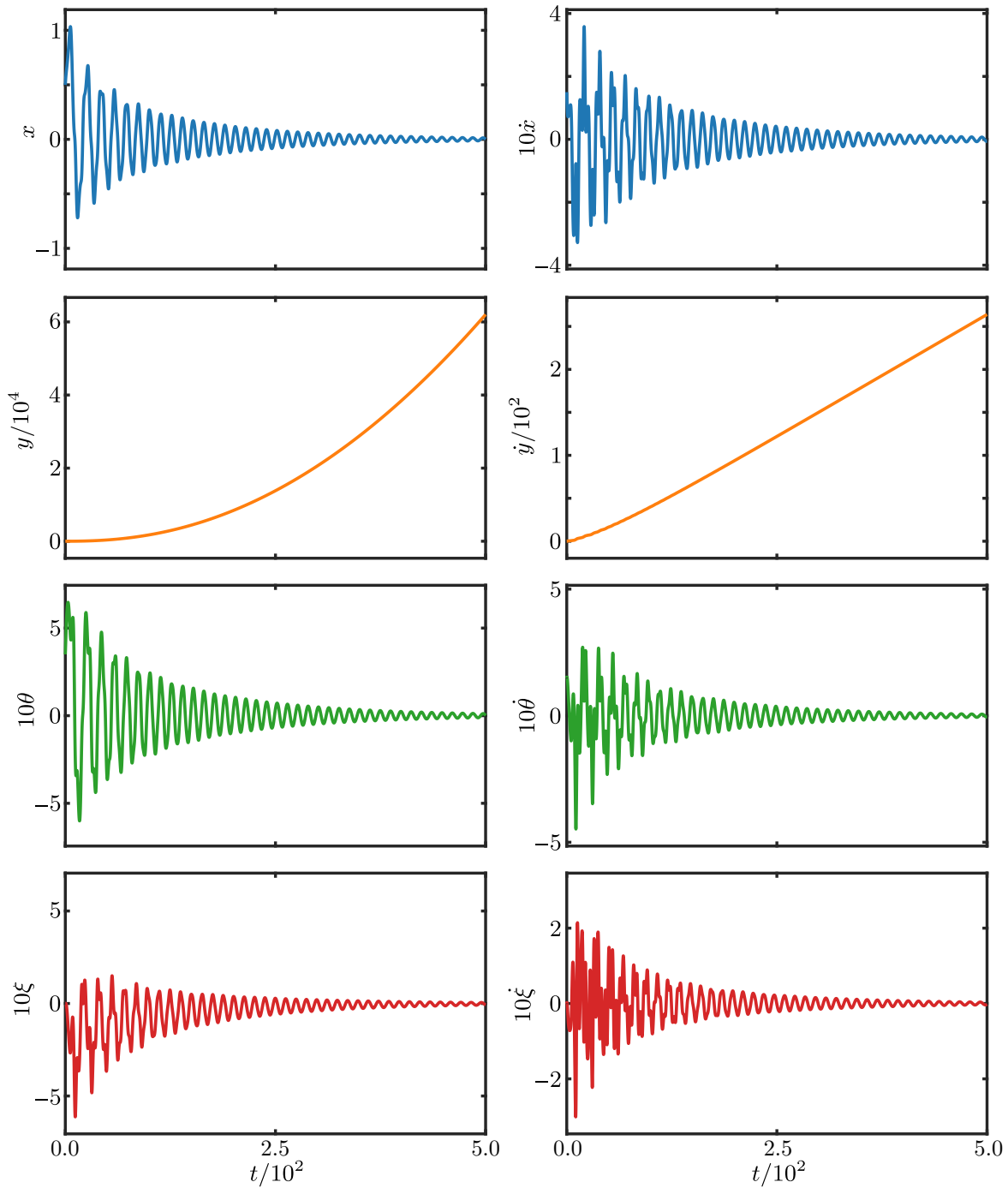


FIG. 4. Dynamics of the MM sail. Elements of  $x, y, \theta, \xi$ , and their derivatives as a function of time  $t$  for parameter values given in column (a) of Fig. 3 with  $\Gamma = 0.04$  and for initial conditions  $(x_0, \theta_0, \dot{x}_0, \dot{\theta}_0) = (0.5, 0.35, 0.15, 0.15)$ .

one parameter at a time. We consider the range of values

$$\begin{aligned}
 0 \leq \delta_0 \leq 0.3, \quad 0.1 \leq \varepsilon \leq 0.4, \quad 0.01 \leq \Gamma \leq 0.1, \\
 1.1 \leq k/k_{\min} \leq 5.6, \quad 1.05 \leq \phi/\phi_{\min} \leq 1.2,
 \end{aligned}
 \tag{8}$$

and, for each parameter, we take seven equally spaced samples except for  $\Gamma$  that is sampled logarithmically. We

divide the initial condition ranges

$$|x_0| \leq 0.15, \quad |\theta_0| \leq 0.15, \quad |\dot{x}_0| \leq 0.15, \quad |\dot{\theta}_0| \leq 0.15,
 \tag{9}$$

into seven equal parts for a total of 2401 sets of initial conditions. We solve the equations of motion by using the

default values for all parameters except one that is varied over the range of values described. For each set of parameter values, we solve the equations of motion for all initial conditions and estimate the damping time (see Appendix A 2).

Figure 5 shows the damping time for  $x$ ,  $\dot{x}$ ,  $\theta$ , and  $\dot{\theta}$  as we vary the parameters  $\delta_0$ ,  $\varepsilon$ ,  $\phi$ ,  $k$ , and  $\Gamma$  while keeping the rest fixed (see the caption for details). Varying  $\delta_0$  [column (a)] has little effect on the damping times. This is not unexpected as  $\delta_0$  varies the intensity, and hence the force of the laser, uniformly. This is counteracted by varying the minimum spring constant  $k_{\min}$  and minimum mirror angle  $\phi_{\min}$  accordingly to adjust the restoring forces on the mirrors and the moveable mass, Eq. (6). Increasing  $\varepsilon$  [column (b)] causes  $\theta$  and  $\dot{\theta}$  to damp more rapidly while producing the opposite effect for  $x$  and  $\dot{x}$ . Increasing  $\phi$  [column (c)] and  $k$  [column (d)] both result in a reduced damping time for all quantities. Changing  $\phi$  affects the restoring

force provided by the laser on the mirrors, while varying  $k$  affects the restoring force on the moveable mass. The interplay of these two restoring forces gives the coupling between the damped degree of freedom and other coordinates and their velocities. Increasing  $\Gamma$  [column (e)] initially results in a reduction of the damping time due to increased damping force; however, as  $\Gamma$  is increased further, the damping times increase. This is as expected and evident from Fig. 3 that shows that the magnitude of the real part of all eigenvalues, except for  $\lambda_6$ , increases with  $\Gamma$  and then decreases.

The results presented in Fig. 5 show only slices of the full parameter space and its effect on damping behavior. Choosing the optimal set of parameter values for a specific metric is nontrivial, as discussed above, and a full analysis of the damping times over the full parameter space is beyond the scope of this paper. However, the inclusion of the damped internal degree of freedom undoubtedly damps

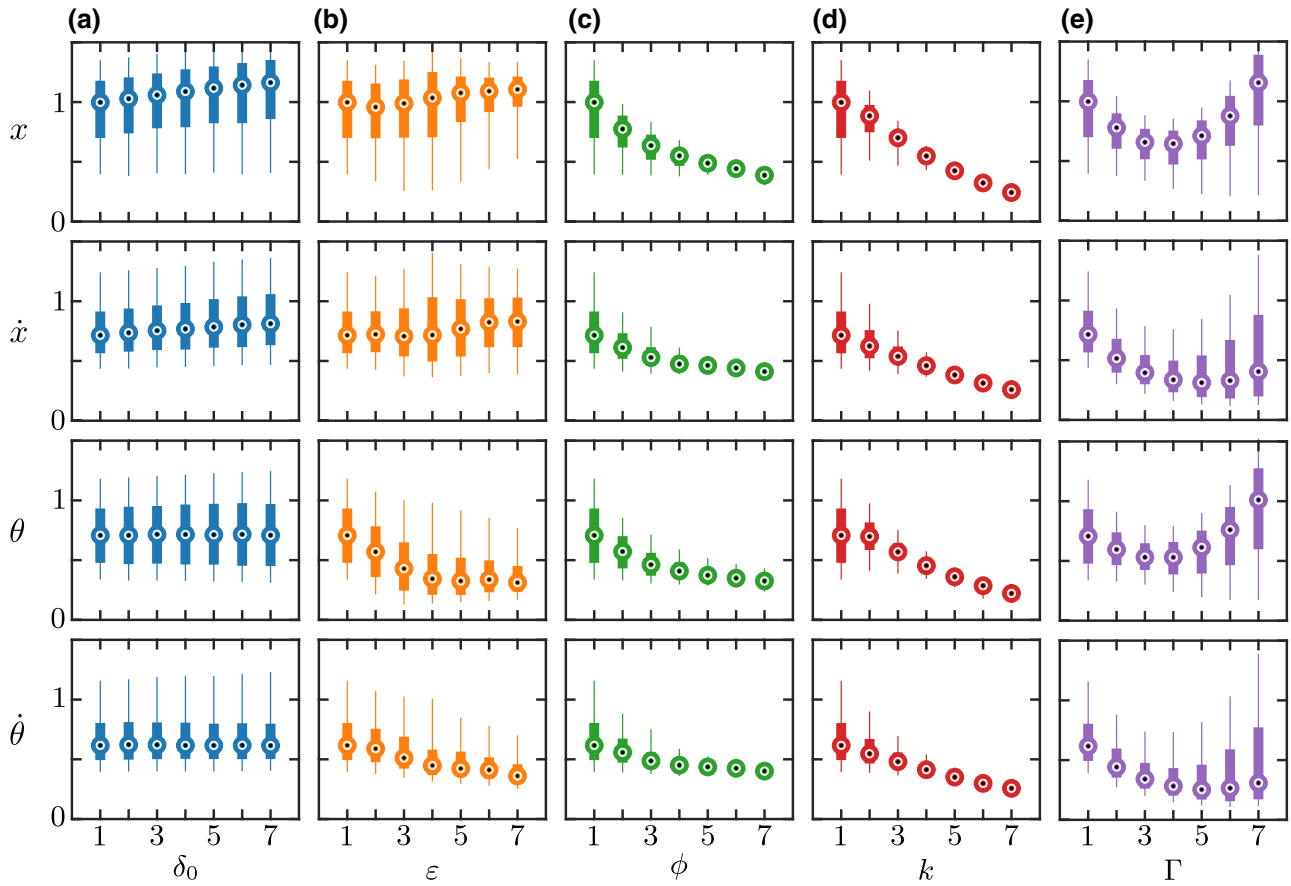


FIG. 5. Damping times as a function of sail and laser parameters. The MM sail is stable for a wide range of parameters and initial perturbations: box-and-whiskers plots of the damping time of  $x$  (first row),  $\dot{x}$  (second row),  $\theta$  (third row), and  $\dot{\theta}$  (fourth row) while varying the parameters (horizontal axes)  $\delta_0$  [column (a)],  $\varepsilon$  [column (b)],  $\phi$  [column (c)],  $k$  [column (d)], and  $\Gamma$  [column (e)] and keeping the rest fixed. Bullseye represents the median; thick portion of the box represents the 25th–75th percentile range; thin lines represent the 5th–95th percentile range. In each cell the leftmost data point is for the default set of parameter values (see the text). All time values have been scaled by the median of the damping time of  $x$  for the default parameter values. The numbers 1 to 7 on the horizontal axes indicate the index of the value of the corresponding parameter below them. All axes are linear except for the horizontal axes of column (e) that is logarithmic owing to the logarithmic sampling of  $\Gamma$ .

the lateral oscillations of the sail in a reasonably small time compared with the total acceleration time of the sail.

## VI. DISCUSSION AND CONCLUSIONS

In this paper we address one of the central challenges in interstellar travel: stability of the sail during its acceleration phase. We modify a simple sail to include a damped internal degree of freedom and demonstrate that the lateral oscillations of the sail may be damped effectively, leading to asymptotic stability of the sail. We give the criteria for asymptotic stability and demonstrate that all small lateral perturbations may be damped effectively for a wide range of sail parameter values. We consider the extra heat generated from the damping of the lateral motions and show that it is likely to be much smaller than the heat generated through absorption of the laser light by the sail (see Appendix E).

We propose and analyze two sails with internal damped degrees of freedom and analyze their ability to damp lateral oscillations of the sail. The designs we discuss are merely two examples of a much larger class. However, they are opposites in that in the MM design the center of mass moves in the direction that connects the two mirrors, whereas in the MA design the center of mass moves perpendicular to this direction. Therefore, even though the MM and MA designs are but two implementations of damped internal degrees of freedom, they each are arguably representative of a much larger set of designs. We may tentatively conclude that, perhaps not surprisingly, the damping of lateral motion requires an internal degree of freedom that can move in the same direction to linear order. This is so even though all of the sails' degrees of freedom are coupled in the equations of motion.

In choosing optimal parameters one might be tempted to consider the equivalent of critical damping, which corresponds to the exceptional point in PT-symmetric systems [40]. However, the condition for critical damping pertains to a single pair of modes ( $\lambda_{5,6}$  in Fig. 3), whereas the other modes are not critically damped. Since the residual motion is determined by the most weakly damped modes ( $\lambda_{1,2}$  in Fig. 3), it may be more advantageous to consider the coalescence points, where accidental degeneracies can lead to the fastest damping.

We have analyzed and discussed the asymptotic stability of the system for a wide range of parameters and initial conditions. An ever present source of perturbations of the sail is the laser beam, including defocusing, and noise in the amplitude and direction of the beam. These imperfections could arise from the laser source or be due to propagation through Earth's atmosphere. If the laser is not focused perfectly on the sail then the beam broadens somewhat and its intensity reduces. Since both of these effects are absorbed in our scaling factors, our conclusions are unaffected by defocusing. If noise is added to the amplitude

and/or the direction of the laser beam then additional analysis would need to be performed. Directional noise may be viewed as the sail starting off center and we have shown that the sail moves to the center of the beam; we cannot yet make statements regarding large and/or rapid variations, which require a separate study. Modest, unbiased noise in the amplitude of the beam has been shown to have a small effect as these fluctuations average out [14]. Sustained, large asymmetries in the beam may be more challenging, but a full analysis of these effects is beyond the scope of the current manuscript. However, they do highlight the need for damping of the perturbations imparted on the light sail during the launch phase.

While our analysis is two dimensional, it can in principle be straightforwardly generalized to three dimensions. This allows not only sideways translation and rotational motion, but also rotation about the axis of the laser beam. The main issue is how to generalize the geometry. One could consider an additional damped mass-spring system orthogonal to the present one, or perhaps  $n$  of these at mutual angles of  $\pi/n$ . All of the geometries shown in Fig. 1 are examples of such generalizations. However, this is outside the scope of the present work. We are confident of the accuracy of our analysis; however, an experimental verification will be challenging and ideally would follow a full 3D analysis.

## ACKNOWLEDGMENTS

We thank Christopher Poulton, Simon Fleming, Peter Tuthill, Sergio Leon-Saval, Stefano Palomba, and Iver Cairns for continued helpful discussions and suggestions. This work is supported by the Science Foundation for Physics and is a Grand Challenge project at the School of Physics, University of Sydney. We thank two anonymous referees for their helpful questions in improving the manuscript.

## APPENDIX A: METHODS

### 1. Equations of motion

The equations of motion of the sails may be obtained using the Newton-Euler approach or using D'Alembert's principle. We derived the equations of motion using both methods and present the latter. The more common Lagrangian or Hamiltonian approaches do not apply here as the force due to the laser does not have an associated potential. D'Alembert's principle gives the equations of motion as [41]

$$\frac{d}{dt} \left( \frac{\partial T}{\partial \dot{q}_j} \right) - \frac{\partial T}{\partial q_j} = Q_j, \quad Q_j = \sum_i \mathbf{F}_i \cdot \frac{\partial \mathbf{x}_i}{\partial q_j}, \quad (\text{A1})$$

where  $\mathbf{F}_i$  is the net nonconstraint force on the mass with position vector  $\mathbf{x}_i$ , the  $q_j$  are generalized coordinates, the  $Q_j$  are generalized forces, with the products  $q_j Q_j$  having

units of energy, and  $T$  is the kinetic energy given by

$$T = \frac{1}{2} \sum_i m_i |\dot{\mathbf{x}}_i|^2. \quad (\text{A2})$$

For the MM sail, we have  $\mathbf{q} = (x, y, \theta, \xi)$  and, for the MA sail,  $\mathbf{q} = (x, y, \theta, \alpha)$ .

## 2. Numerical results

The equations of motion are solved using the MATLAB<sup>®</sup> built-in solver *ode113* with an absolute and relative error tolerance of  $5 \times 10^{-14}$ . The damping times are estimated by fitting a curve to the envelope of the absolute values of  $\mathbf{q}$  and  $\dot{\mathbf{q}}$ . The eigenvalues are calculated numerically using built-in MATLAB functions.

## 3. Nominal parameter values

To obtain a nominal set of parameter values, we consider a 3D sail with mass  $m_{\text{sail}} = 10^{-3}$  kg and surface area  $A_{\text{sail}} = 10 \text{ m}^2$ , subject to a laser beam with uniform intensity profile, that has an intensity such that it accelerates the sail, under perfect specular reflection at normal incidence and ignoring relativistic effects, to  $0.2c$  in 15 min. The sail then has surface mass density  $\rho_{\text{sail}} = m_{\text{sail}}/A_{\text{sail}} = 10^{-4}$  kg/m. Assuming similar acceleration for the MM sail with nominal  $A = 10^{-2} \text{ m}^2$ ,  $L = 1$  m,  $m_1 = A\rho_{\text{sail}}$ ,  $\delta_0 = 0.1$ ,  $\varepsilon = 0.1$ ,  $\phi = 1.15\phi_{\text{min}}$ , and  $\ddot{y} = 2(1 + \delta_0) \cos^3 \phi$  requires that  $I_0 \approx 3.9 \times 10^9 \text{ W/m}^2$ . These give nominal scaling parameters

$$\begin{aligned} m_s &\approx 2.2 \times 10^{-6} \text{ kg}, & x_s &= 1 \text{ m}, & t_s &\approx 2.9 \times 10^{-3} \text{ s}, \\ k_s &\approx 0.26 \text{ kg/s}^2, & \Gamma_s &\approx 7.6 \times 10^{-4} \text{ kg/s}. \end{aligned} \quad (\text{A3})$$

## APPENDIX B: SIMPLE SAIL

The characteristic polynomial of the simple sail may be obtained from linearizing its equations of motion or from Eq. (D1) below by taking the limits  $\bar{k}/\varepsilon \rightarrow 0$ ,  $\bar{\Gamma}/\varepsilon \rightarrow 0$ , and  $\varepsilon \rightarrow 0$  as

$$\begin{aligned} P(\lambda) &= \lambda^2[\lambda^4 + \Lambda_4\lambda^2 + \Lambda_2], \\ \Lambda_4 &= 4(2 + \delta_0) \cos^2 \phi \sin \phi, & \Lambda_2 &= 8(1 + \delta_0) \cos^6 \phi, \end{aligned} \quad (\text{B1})$$

with nontrivial solutions

$$\lambda = \pm \left\{ -\frac{\Lambda_4}{2} [1 \pm \Delta^{1/2}] \right\}^{1/2}, \quad \Delta = 1 - \frac{4\Lambda_2}{\Lambda_4^2}. \quad (\text{B2})$$

The system is marginally stable (i.e., all eigenvalues are purely imaginary) when  $0 \leq \Delta \leq 1$ , which is satisfied

provided we have

$$\phi_{\text{min}} \leq \phi \leq \frac{\pi}{2}, \quad \phi_{\text{min}} = \tan^{-1} \left[ \frac{\sqrt{2(1 + \delta_0)}}{2 + \delta_0} \right], \quad (\text{B3})$$

and the system is unstable otherwise.

## APPENDIX C: MOVING ARMS SAIL

The equations of motion of the MA sail, shown in Fig. 2(c), may be obtained using Eq. (A1) as follows. We have

$$\begin{aligned} \mathbf{x}_{L,R} &= \mathbf{x}_c \mp L \sin \alpha \hat{\mathbf{r}}, \\ \hat{\mathbf{n}}_{L,R} &= [\mp \cos(\alpha \pm \theta - \phi), -\sin(\alpha \pm \theta - \phi)]. \end{aligned} \quad (\text{C1})$$

The force due to the laser is given by Eq. (3) and by the force exerted by the torsion spring on the two mirrors of the MA sail

$$\begin{aligned} \mathbf{F}_{sL,R} &= [k(\alpha_0 - \alpha) - \Gamma\dot{\alpha}] \hat{\mathbf{n}}_{L,R}, \\ \hat{\mathbf{n}}_{L,R} &= [\mp \cos(\alpha \pm \theta), -\sin(\alpha \pm \theta)], \end{aligned} \quad (\text{C2})$$

where the unit normals to the arms, as shown in Fig. 2(c). The nondimensional equations of motion for the MA sail are then obtained as

$$\begin{aligned} \ddot{x} &= \bar{I}(\mathbf{x}_L) \sin^2(\alpha + \theta - \phi) \cos(\alpha + \theta - \phi) \\ &\quad - \bar{I}(\mathbf{x}_R) \sin^2(\alpha - \theta - \phi) \cos(\alpha - \theta - \phi) \\ &\quad + \sin \alpha \sin \theta [\bar{k}(\alpha_0 - \alpha) - \bar{\Gamma}\dot{\alpha}], \end{aligned} \quad (\text{C3a})$$

$$\begin{aligned} \ddot{y} &= \bar{I}(\mathbf{x}_L) \sin^3(\alpha + \theta - \phi) + \bar{I}(\mathbf{x}_R) \sin^3(\alpha - \theta - \phi) \\ &\quad - \sin \alpha \cos \theta [\bar{k}(\alpha_0 - \alpha) - \bar{\Gamma}\dot{\alpha}], \end{aligned} \quad (\text{C3b})$$

$$\begin{aligned} \ddot{\theta} &= -2 \cot \alpha \dot{\alpha} \dot{\theta} - \frac{\sin(\alpha - \phi)}{\sin \alpha} [\bar{I}(\mathbf{x}_L) \sin^2(\alpha + \theta - \phi) \\ &\quad - \bar{I}(\mathbf{x}_R) \sin^2(\alpha - \theta - \phi)], \end{aligned} \quad (\text{C3c})$$

$$\begin{aligned} \ddot{\alpha} &= \tan \alpha (\dot{\alpha}^2 + \dot{\theta}^2) + [\bar{k}(\alpha_0 - \alpha) - \bar{\Gamma}\dot{\alpha}] \\ &\quad - \frac{\cos(\alpha - \phi)}{\cos \alpha} [\bar{I}(\mathbf{x}_L) \sin^2(\alpha + \theta - \phi) \\ &\quad + \bar{I}(\mathbf{x}_R) \sin^2(\alpha - \theta - \phi)], \end{aligned} \quad (\text{C3d})$$

where we nondimensionalize using  $m_s = m_1$ ,  $x_s = L$ ,  $t_s = \sqrt{MLC/I_0A}$ ,  $k_s = m_s x_s / t_s^2$ , and  $\Gamma_s = m_s x_s / t_s$ . Again, we drop the bar on the nondimensionalized parameters for simplicity of notation.

Unlike Eq. (5) we observe that, for the MA sail, the spring force couples directly to the  $x$  and  $y$  coordinates in addition to the internal degree of freedom  $\alpha$ . The Coriolis effect [first term of Eq. (C3c)] and centrifugal effect [first term of Eq. (C3d)] are again present. The singularity in the equations of motion of the MA sail at  $\alpha = \pi/2$  can be

removed if we add a nonzero mass at the hinge, as discussed above. This additional mass would regularize the equations of motion without affecting the stability of the system. We choose  $0 < \alpha_0 < \pi$  but sufficiently away from  $\pi/2$  so that the oscillations of the arms about  $\alpha = \alpha_0$  do not cross  $\alpha = \pi/2$ .

Linearizing the equations of motion about the equilibrium point  $(x, \theta, \alpha, \dot{x}, \dot{\theta}, \dot{\alpha}) = (0, 0, \alpha_0, 0, 0, 0)$  gives a characteristic polynomial of the form

$$P(\lambda) = \lambda^2[\lambda^2 + \Lambda_{11}\lambda + \Lambda_{10}][\lambda^4 + \Lambda_{21}\lambda^2 + \Lambda_{22}], \quad (\text{C4})$$

which may be solved directly. The only set of solutions where there are no eigenvalues with a nonzero positive real part are

$$\begin{aligned} \lambda_{1,2} &= -\frac{1}{2}\Gamma \left\{ 1 \pm \sqrt{1 - 4(k + \Delta_1)/\Gamma^2} \right\}, \\ \lambda_{3-6} &= \pm i\Delta_2 \left\{ 1 \pm \sqrt{\Delta_3} \right\}^{1/2}, \end{aligned} \quad (\text{C5})$$

subject to  $k + \Delta_1 \geq 0$ ,  $\Delta_2 \geq 0$ , and  $\Delta_3 \geq 0$ , where

$$\begin{aligned} \Delta_1 &= \left( \frac{3}{2} + 2\delta_0 \right) \sin(2\alpha_0 - 3\phi) - \sin(4\alpha_0 - 3\phi) \\ &\quad + \frac{1}{2} \sin(2\alpha_0 - \phi) + 2(1 + \delta_0) \frac{\cos^2 \phi}{\cos^2 \alpha_0} \sin \phi, \end{aligned} \quad (\text{C6a})$$

$$\Delta_2 = 4 \left( 1 + \frac{\delta_0}{2 \sin^2 \alpha_0} \right) \sin \alpha_0 \sin^2(\alpha_0 - \phi) \cos(\alpha_0 - \phi), \quad (\text{C6b})$$

$$\Delta_3 = 1 - \frac{\tan^2(\alpha_0 - \phi)[1 + \delta_0 \csc^2 \alpha_0]}{2(1 + \delta_0 \csc^2 \alpha_0/2)^2}. \quad (\text{C6c})$$

Two of the eigenvalues have negative real parts and four eigenvalues are purely imaginary. We note that the damping coefficient  $\Gamma$  only enters the expression for  $\lambda_{1,2}$  and does not appear in the expressions for  $\lambda_{3-6}$ . Mathematically, the characteristic polynomial factors indicate that there is block diagonalization, and hence the dissipation does not couple to all degrees of freedom. Thus, not all perturbations of the MA sail damp over time. The equations of motion of the MA sail are more nonlinear compared to those of the MM sail, as is evident from Eqs. (5) and (C3). This is likely to lead to faster growth of perturbations of the sail due to nonlinear effects. Therefore, designs based on the MA sail are not viable if one intends to damp out all lateral perturbations of the sail.

## APPENDIX D: MM SAIL CHARACTERISTIC POLYNOMIAL

The characteristic polynomial of the MM sail is obtained from the Jacobian matrix of Eq. (5) as

$$P(\lambda) = \lambda^2[\lambda^6 + \Lambda_5\lambda^5 + \Lambda_4\lambda^4 + \Lambda_3\lambda^3 + \Lambda_2\lambda^2 + \Lambda_1\lambda + \Lambda_0] \quad (\text{D1})$$

with coefficients

$$\Lambda_0 = \frac{16(1 + \delta_0) \cos^6 \phi \{k - (1 + \delta_0)\varepsilon^2 \cos^2 \phi \sin \phi\}}{\varepsilon(1 - \varepsilon)^2}, \quad (\text{D2a})$$

$$\Lambda_1 = \frac{16\Gamma(1 + \delta_0) \cos^6 \phi}{\varepsilon(1 - \varepsilon)^2}, \quad (\text{D2b})$$

$$\begin{aligned} \Lambda_2 &= \frac{8(1 + \delta_0) \cos^4 \phi \{(1 + \delta_0\varepsilon) \cos^2 \phi - (1 + \delta_0)\varepsilon\}}{(1 - \varepsilon)^2} \\ &\quad + \frac{8k(2 + \delta_0 - \varepsilon) \cos^2 \phi \sin \phi}{\varepsilon(1 - \varepsilon)^2}, \end{aligned} \quad (\text{D2c})$$

$$\Lambda_3 = \frac{8\Gamma(2 + \delta_0 - \varepsilon) \cos^2 \phi \sin \phi}{\varepsilon(1 - \varepsilon)^2}, \quad (\text{D2d})$$

$$\Lambda_4 = \frac{2k + 4(2 + \delta_0)\varepsilon \cos^2 \phi \sin \phi}{\varepsilon(1 - \varepsilon)}, \quad (\text{D2e})$$

$$\Lambda_5 = \frac{2\Gamma}{1 - \varepsilon}. \quad (\text{D2f})$$

## APPENDIX E: DISSIPATED ENERGY

We demonstrated that all lateral perturbations in coordinates  $x$ ,  $\theta$ , and their time derivatives for the MM sail are damped. The dissipated energy is additional heat that can only be (meaningfully) lost through thermal radiation. Cooling of the sail is a difficult task in itself [11] and, as such, the damping mechanism must produce as little additional heat as possible. Here we discuss the rate of heat production by the damping mechanism of the MM sail and compare it to the expected heating of the sail through absorption of the laser light.

The total energy incident on the sail from the laser beam in time  $t$  is

$$E_L(t) = -\frac{ct_s}{2L} \sum_{i=L,R} \int_0^t I(\mathbf{x}_i) (\hat{\mathbf{n}}_i \cdot \hat{\mathbf{y}}) dt'. \quad (\text{E1})$$

An actual sail absorbs energy  $a_\alpha E_L(t)$ , where  $a_\alpha$  is the total absorption coefficient. We wish to compare the heat generated by damping of the lateral oscillations of the sail to this absorbed energy from the laser. The heat generated by damping is given by the work done by the moveable mass

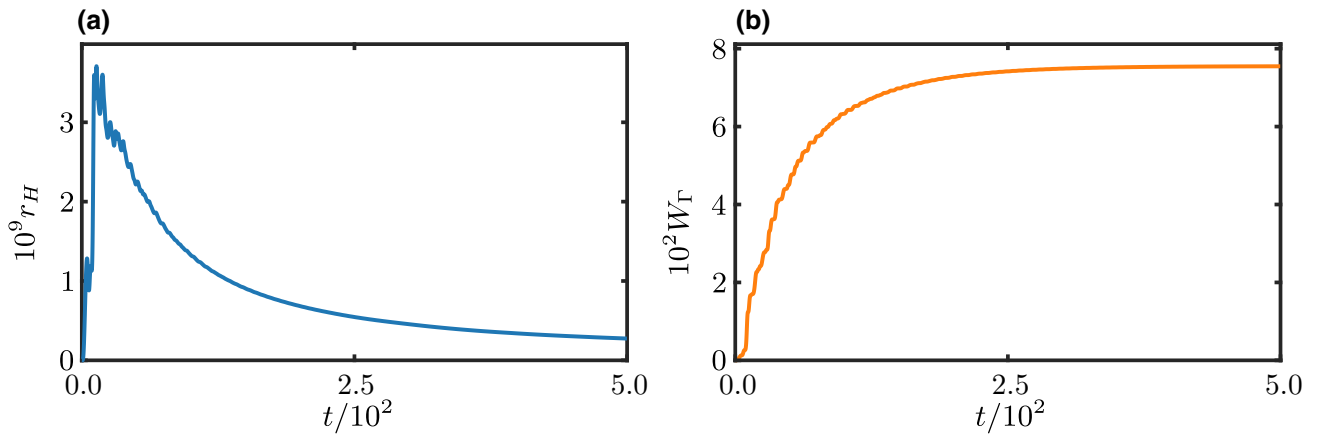


FIG. 6. Estimates of the heat dissipation in the sail and comparison to absorbed energy from the incident laser beam. Plots of (a)  $r_H$  and (b)  $W_\Gamma$  versus time  $t$  for the same parameter values and initial conditions as in Fig. 4.

against the damping force

$$W_\Gamma(t) = 2\Gamma \int_0^t \dot{\xi}^2 dt, \quad (\text{E2})$$

where we have used Eq. (4). The ratio of thermal energy due to damping of the lateral motion to absorbed laser energy is  $r_h = r_H/r_\alpha$ , where

$$r_H = \frac{W_\Gamma(t)}{E_L(t)}. \quad (\text{E3})$$

Figure 6 shows (a)  $r_H$  and (b)  $W_\Gamma$  versus time for the parameters in Fig. 4. The total heat produced due to damping is approximately  $7.55 \times 10^{-2}$ , which is smaller than

the total laser energy landing on the sail by a factor of approximately  $7.9 \times 10^9$ , as shown by the plot of  $r_H$ . The rate of heat generation through damping is largest in the early stages of motion where lateral perturbations are largest. As the perturbations damp, the rate of heat generated drops as well. At its peak, the heat generated through damping is equivalent to a total absorption factor of approximately  $3.71 \times 10^{-9}$ . Reasonable total absorption for candidate sail materials is  $a_\alpha \gtrsim 10^{-8}$  [6], which is significantly higher than the heat generated through damping of the lateral oscillations of the sail. In addition to this, the sets of initial conditions chosen in Figs 4 and 6 are quite extreme. In reality, we expect milder perturbations of the sail and hence a reduced rate of heat generation due to the damping of the lateral perturbations of the sail.

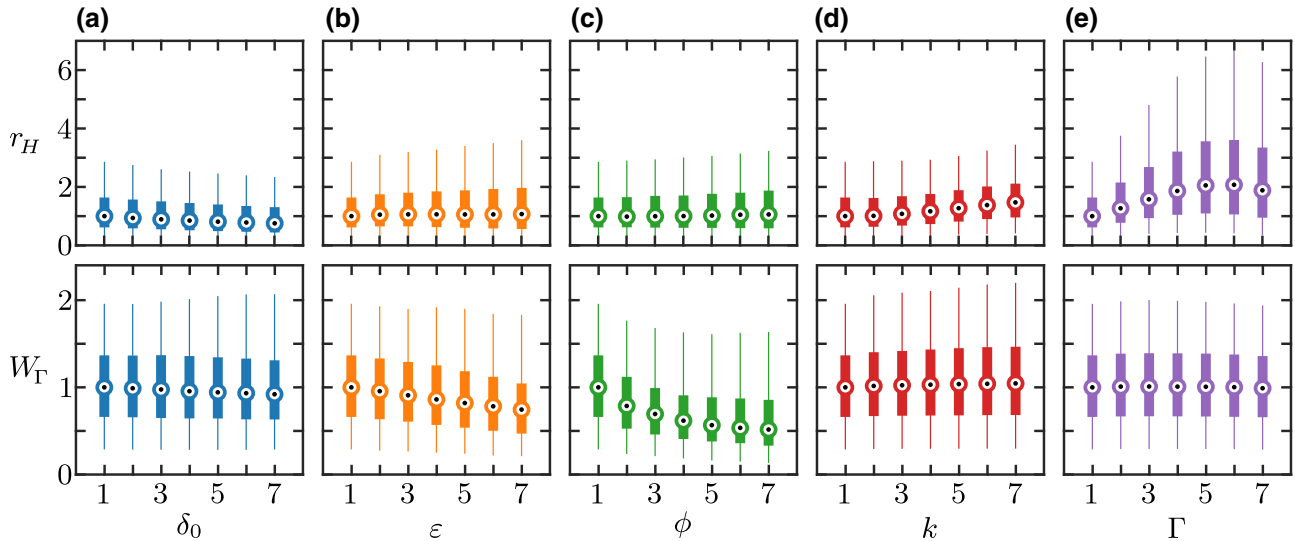


FIG. 7. Heat generated as a function of sail and laser parameters. Box-and-whiskers plots of values of  $r_H$  (top row), scaled by  $5.25 \times 10^{-11}$ , and  $W_\Gamma$  (bottom row), scaled by  $3.10 \times 10^{-2}$ , while varying parameters (horizontal axes)  $\delta_0$  [column (a)],  $\epsilon$  [column (b)],  $\phi$  [column (c)],  $k$  [column (d)], and  $\Gamma$  [column (e)] and keeping the rest fixed. See the caption of Fig. 5 for further details.

## 1. Numerical results

We analyze the rate of heat generation by calculating the maximum value of  $r_H$  and the total heat  $W_\Gamma$  generated through damping for the same setup as discussed in the main text

Figure 7 shows box-and-whiskers plots of the values of  $r_H$  (top row) and  $W_\Gamma$  (bottom row) as described in the figure caption. We observe that the rate of heat production depends most strongly on  $k$  and  $\Gamma$  and that the total amount of heat produced varies appreciably only when  $\phi$  is changed. Larger  $k$  and  $\Gamma$  result in a greater rate of heat production, unsurprisingly, as  $\Gamma$  is directly responsible for heat production and larger  $k$  means larger  $\xi$  and hence a larger rate of heat production.

- 
- [1] Breakthrough Starshot Initiative. URL <https://breakthroughinitiatives.org/Initiative/3> (Accessed: 2021-06-12).
- [2] Parker solar probe (2018). URL [https://www.nasa.gov/sites/default/files/atoms/files/parkersolarprobe\\_presskit\\_august\\_2018\\_final.pdf](https://www.nasa.gov/sites/default/files/atoms/files/parkersolarprobe_presskit_august_2018_final.pdf). (Accessed: 2021-06-12).
- [3] G. Marx, Interstellar vehicle propelled by terrestrial laser beam, *Nature* **211**, 22 (1966).
- [4] R. L. Forward, Roundtrip interstellar travel using laser-pushed lightsails, *J. Spacecr. Rockets* **21**, 187 (1984).
- [5] P. Lubin, A roadmap to interstellar flight, *J. Br. Interplanet. Soc.* **69**, 40 (2016).
- [6] Harry A. Atwater, Artur R. Davoyan, Ognjen Ilic, Deep Jariwala, Michelle C. Sherrott, Cora M. Went, William S. Whitney, and Joelson Wong, Materials challenges for the Starshot lightsail, *Nat. Mater.* **17**, 861 (2018).
- [7] Chathura P. Bandutunga, Paul G. Sibley, Michael J. Ireland, and Robert L. Ward, Photonic solution to phase sensing and control for light-based interstellar propulsion, *J. Opt. Soc. Am. B* **38**, 1477 (2021).
- [8] Artur R. Davoyan, Jeremy N. Munday, Nelson Tabiryan, Grover A. Swartzlander, and Les Johnson, Photonic materials for interstellar solar sailing, *Optica* **8**, 722 (2021).
- [9] Ognjen Ilic and Harry A. Atwater, Self-stabilizing photonic levitation and propulsion of nanostructured macroscopic objects, *Nat. Photonics* **13**, 289 (2019).
- [10] Weiliang Jin, Wei Li, Meir Orenstein, and Shanhui Fan, Inverse design of lightweight broadband reflector for relativistic lightsail propulsion, *ACS. Photonics* **7**, 2350 (2020).
- [11] Ognjen Ilic, Cora M. Went, and Harry A. Atwater, Nanophotonic heterostructures for efficient propulsion and radiative cooling of relativistic light sails, *Nano Lett.* **18**, 5583 (2018).
- [12] David G. Messerschmitt, Philip Lubin, and Ian Morrison, Challenges in scientific data communication from low-mass interstellar probes, *Astrophys. J. Suppl. Ser.* **249**, 36 (2020).
- [13] Prateek R. Srivastava, Ying-Ju Lucy Chu, and Grover A. Swartzlander, Stable diffractive beam rider, *Opt. Lett.* **44**, 3082 (2019).
- [14] Mohammad Mahdi Salary and Hossein Mosallaei, Photonic metasurfaces as relativistic light sails for doppler-broadened stable beam-riding and radiative cooling, *Laser Photonics Rev.* **14**, 1900311 (2020).
- [15] Zachary Manchester and Abraham Loeb, Stability of a light sail riding on a laser beam, *Astrophys. J. Lett.* **837**, L20 (2017).
- [16] Joel Siegel, Anthony Y. Wang, Sergey G. Menabde, Mikhail A. Kats, Min Seok Jang, and Victor Watson Brar, in *OSA Advanced Photonics Congress (AP) 2019 (IPR, Networks, NOMA, SPPCom, PVLED)* (Optical Society of America, Burlingame, California, United States, 2019), p. JW4A.1.
- [17] Elena Popova, Messoud Efendiev, and Ildar Gabitov, On the stability of a space vehicle riding on an intense laser beam, *Math. Methods Appl. Sci.* **40**, 1346 (2017).
- [18] Edl Schamiloglu, Chaouki T. Abdallah, Kristina A. Miller, Daniel Georgiev, James Benford, Gregory Benford, and Gurkirpal Singh, in *Space Technology and Applications International Forum—2001*, edited by Mohamed S. El-Genk, American Institute of Physics Conference Series, Vol. 552 (AIP Conference Proceedings, Albuquerque, New Mexico, United States, 2001), p. 559.
- [19] Karthik Vijay Myilswamy, Aravind Krishnan, and Michelle L. Povinelli, Photonic crystal lightsail with nonlinear reflectivity for increased stability, *Opt. Express* **28**, 8223 (2020).
- [20] Yoshikazu Kitagawa and Mitsumasa Midorikawa, Seismic isolation and passive response-control buildings in Japan, *Smart Mater. Struct.* **7**, 581 (1998).
- [21] Aly Mousaad Aly, Proposed robust tuned mass damper for response mitigation in buildings exposed to multi-directional wind, *Struct. Des. Tall Spec. Build.* **23**, 664 (2014).
- [22] Interplanetary kite-craft accelerated by radiation of the sun (ikaros). URL <https://global.jaxa.jp/projects/sas/ikaros/> (Accessed: 2021-06-18).
- [23] M. Duocastella and C. B. Arnold, Bessel and annular beams for materials processing, *Laser Photonics Rev.* **6**, 607 (2012).
- [24] Miles Padgett, Johannes Courtial, and Les Allen, Light's orbital angular momentum, *Phys. Today* **57**, 35 (2004).
- [25] Neeraj Kulkarni, Philip Lubin, and Qicheng Zhang, Relativistic spacecraft propelled by directed energy, *Astron. J. (N. Y.)* **155**, 155 (2018).
- [26] David Kipping, Relativistic light sails, *Astron. J. (N. Y.)* **153**, 277 (2017).
- [27] Johanna Bible, Isabella Johansson, Gary B. Hughes, and Philip M. Lubin, in *Nanophotonics and Macrophotonics for Space Environments VII*, edited by Edward W. Taylor and David A. Cardimona, Society of Photo-Optical Instrumentation Engineers (SPIE) Conference Series, Vol. 8876 (SPIE, San Diego, California, United States, 2013), p. 887605.
- [28] Manasvi Lingam and Abraham Loeb, Propulsion of spacecraft to relativistic speeds using natural astrophysical sources, *Astrophys. J.* **894**, 36 (2020).
- [29] André Füzfa, Williams Dhelonga-Biarufu, and Olivier Welcomme, Sailing towards the stars close to the speed of light, *Phys. Rev. Res.* **2**, 043186 (2020).
- [30] I. S. Gradshteyn, I. M. Ryzhik, Alan Jeffrey, and Daniel Zwillinger, *Table of Integrals, Series, and Products* (Elsevier, Academic Press, 2007).

- [31] Carl M. Bender and Stefan Boettcher, Real Spectra in non-Hermitian Hamiltonians Having PT Symmetry, *Phys. Rev. Lett.* **80**, 5243 (1998).
- [32] Mohammad-Ali Miri and Andrea Alù, Exceptional points in optics and photonics, *Science* **363**, eaar7709 (2019).
- [33] Sergey V. Suchkov, Andrey A. Sukhorukov, Jiahao Huang, Sergey V. Dmitriev, Chaohong Lee, and Yuri S. Kivshar, Nonlinear switching and solitons in PT-symmetric photonic systems, *Laser Photonics Rev.* **10**, 177 (2016).
- [34] Alessandro Tuniz, Torsten Wieduwilt, and Markus A. Schmidt, Tuning the Effective  $\mathcal{PT}$  Phase of Plasmonic Eigenmodes, *Phys. Rev. Lett.* **123**, 213903 (2019).
- [35] W. D. Heiss, The physics of exceptional points, *J. Phys. A Math. Gen.* **45**, 444016 (2012).
- [36] W. D. Heiss and H. L. Harney, The chirality of exceptional points, *Eur. Phys. J. D* **17**, 149 (2001).
- [37] W. D. Heiss, Repulsion of resonance states and exceptional points, *Phys. Rev. E* **61**, 929 (2000).
- [38] M. S. Rudner and L. S. Levitov, Topological Transition in a Non-Hermitian Quantum Walk, *Phys. Rev. Lett.* **102**, 065703 (2009).
- [39] Liang Feng, Ye-Long Xu, William S. Fegadolli, Ming-Hui Lu, José E. B. Oliveira, Vilson R. Almeida, Yan-Feng Chen, and Axel Scherer, Experimental demonstration of a unidirectional reflectionless parity-time metamaterial at optical frequencies, *Nat. Mater.* **12**, 108 (2013).
- [40] Francisco M. Fernández, Exceptional point in a simple textbook example, *Eur. J. Phys.* **39**, 045005 (2018).
- [41] H. Goldstein, C. Poole, and J. Safko, *Classical Mechanics* (Addison-Wesley, San Francisco, 2002).